A Novel Plasmonic Nanoantenna-Based Sensor for Illicit Materials and Drugs Detection

Marco Scalici and Patrizia Livreri, *Senior Member, IEEE*

***Abstract*—Terahertz (THz) spectroscopy and imaging are of significant interest in molecular detection and identification. Illicit drugs are characterized by a different absorption spectrum, with sharp absorption peaks located in the THz frequency range. In this article, the design, simulation, and fabrication of two novel plasmonic nanoantennas with resonance frequencies over the 1–10-THz range for illicit materials and drugs detection are proposed. The first nanoantenna, called the butterfly nanoantenna, is composed of two symmetrical butterfly shaped gold arms with a length of 46.48 μm, a width of 22.40 μm, and a thickness of 200 nm, separated by a gap of 20 nm. The two-layer substrate consists of 3-μm silicon and 50-nm gold. The results of the simulation, performed by the 3-D CST Studio Suite 2023, show three different resonance frequencies at 2.1, 3.6, and 5.1 THz, respectively, with a −10-dB S_{11} lower than −18 dB and a directivity of up to 11.04 dBi. Starting from the single butterfly nanoantenna design, a novel geometrical nanoantenna, called the shamrock nanoantenna, is composed of three symmetrical arms, each with a length of 23.14 μm, a width of 22.40 μm, and a thickness of 200 nm, separated by a central gap of 20 nm is introduced. The simulation results show two different resonance frequencies at 1.9 and 3.3 THz, with −10-dB S_{11} lower than −26 and −20 dB, respectively. A sensitivity of 1500 GHz/RIU at 1.9 THz, 2500 GHz/RIU at 2.1 THz, 6000 GHz/RIU at 3.3 THz, 10 000 GHz/RIU at 3.6 THz, and 11 500 GHz/RIU at 5.1 THz is theoretically observed for the detection of illicit materials and drugs with a thickness of 5 μm of analyte. The multiband sensor based on the proposed plasmonic nanoantennas with an enhancement factor (EF) of 6.09 × 10^5 shows a very broad observation range providing a nondestructive method.**

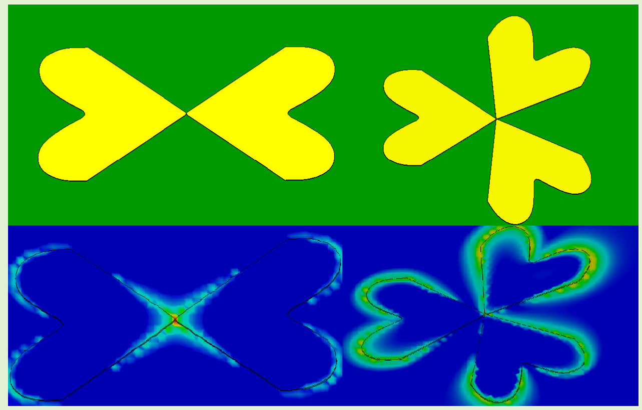

***Index Terms*— Drugs, illicit materials, nanoantenna, plasmonics, sensor, terahertz (THz).**

I. Introduction

RECENTLY, growing interest in the localization and amplification of electromagnetic fields on plasmonic surfaces in the near-field region has been attributed to their promising applications, including energy deposition, refractive index sensors, and spectroscopic hotspots. In particular, in the frequency range of 1–10 THz, numerous potential applications in the security and defense sectors have emerged owing to extensive exploration and notable advances in terahertz (THz) radiation.

Many materials relevant to security applications, including explosives and chemical and biological agents, exhibit characteristic THz spectra that can be used to identify illegal substances. With the increasing use of plastic explosives and chemical and biological agents, such as weapons of war and terrorism, and the growing threat of illegal drug trafficking, effective means for the rapid detection and identification of these threats are indispensable [1]. For example, numerous explosives (e.g., HMX, SEMTEX-H, and TNT) and illegal drugs (e.g., methylenedioxymethamphetamine (MDMA), heroin, and cocaine) exhibit distinctive transmission and reflection spectra in the THz frequency range [2]. In Table I, the resonance frequencies of some illicit materials and drugs occurring over the 1.9–5.1-THz range have been reported [3], [4].

TABLE I
Resonance Frequency at THz of Illicit Materials and Drugs

Frequency (THz)	Illicit materials and drugs
1.9	PE4, HMX, TNT, MDMA
2.1	SEMTEX-H
3.3	Lactose a-monohydrate, Terfenadine
3.6	Co-Codamol
5.1	Naproxen sodium, Caffeine

Manuscript received 7 June 2024; revised 10 July 2024; accepted 13 July 2024. The associate editor coordinating the review of this article and approving it for publication was Dr. Amir Ebrahimi. *(Corresponding author: Patrizia Livreri.)*

The authors are with the Department of Engineering, University of Palermo, 90128 Palermo, Italy (e-mail: marco.scalici@community.unipa.it; patrizia.livreri@unipa.it).

Digital Object Identifier 10.1109/JSEN.2024.3429154

Because different substances have different absorption intensities and wavelengths, their absorption peaks and reflected intensities in infrared spectroscopy vary [5]. Spectroscopy technology is increasingly being used in biomedical research owing to its speed and nondestructive detection, and it can work very well for the detection of various molecules, such as illicit drugs or explosives [6].

The application of THz spectroscopy and imaging in the detection and identification of illicit substances based on plasmonic nanoantennas allows nondestructive sensing.

A plasmonic nanoantenna is a nanometric device designed to exploit the phenomenon of surface plasmons, which are the collective oscillations of electrons that propagate along the metallic surface of a conductive material when excited by an electromagnetic field. When the wavelength of the incident light coincides with the wavelength of the nanoantenna plasmon resonance, a significant increase in the light absorption or its interaction with the nanostructure occurs [7].

Plasmonic nanoantennas are mainly used to manipulate light at the nanometer level for applications, such as highly sensitive chemical and biological sensors, advanced imaging technologies, such as plasmon microscopy, and advanced optical devices, such as super-resolution lenses and nanoscale light sources [8].

Plasmonics studies have led to the use of nanoantenna dipoles with two or four arms [9], [10], or, at most, the classic bowtie [11] for the detection of different molecules, which facilitates the design of simple shapes to be designed and fabricated in the laboratory. However, the classic bowtie does not allow obtaining a sensor for the detection of all resonance frequencies reported in Table I.

In this study, we propose novel geometric nanoantennas operating at THz frequencies that exhibit optimal characteristics in terms of high electromagnetic-field enhancement, directivity, and reflectivity. Inspired by the geometry of a bowtie antenna [12] composed of two triangular arms, these novel geometries have been demonstrated to be effectiveness in the near-infrared domain.

The remainder of this article is organized as follows. Section II presents the design, simulations, and parametric analyses of butterfly nanoantennas. Section III reports the simulations of the 2 $\times$ 2 butterfly nanoarrays. In Section IV, starting with the butterfly nanoantenna, the design and simulations of the proposed shamrock nanoantenna are presented in detail. Shamrock nanoantenna array simulations are presented in Section V. Section VI compares butterfly and shamrock nanoantennas with the classic bowtie and three-arm bowtie nanoantennas, and Q-factor values are reported. Section VII discusses the sensitivity of the novel nanoantennas and the application of the nanoantenna array as a naked sensor. Finally, the conclusions are presented in Section VIII.

II. Butterfly Plasmonic Nanoantenna Design

Fig. 1 shows a schematic model of the butterfly nanoantenna composed of two gold arms of length L, width W, and flare angle Θ, separated by a gap G. A two-layer substrate, composed of silicon and gold, was used.

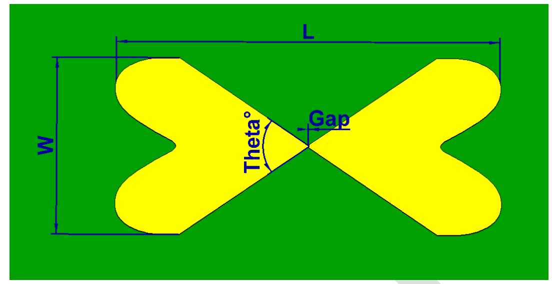

Fig. 1. CST schematic model of the butterfly nanoantenna.

According to Maxwell's equations and the properties of materials, at RF/microwave resonance frequency, the length L of a generic dipole antenna is given by

$$L = \frac{\lambda}{2} = \frac{c}{f \times \sqrt{\epsilon_{\text{eff}}}} \quad (1)$$

with λ the wavelength of the electromagnetic waves, c the speed of light, f the antenna operating frequency, and ϵ_{eff} the dielectric constant.

Therefore, antenna size depends on the wavelength of the incident wave. Moreover, owing to the infinite conductivity of metals, the skin depth is irrelevant with respect to the size of the antenna. When a circularly polarized plane wave along the z-axis with an arbitrary electric-field intensity interacts with an antenna, it induces electron oscillations at the metal–dielectric interface.

These electron oscillations at the frequency of the incident wave are referred to as surface plasmon polaritons (SPPs). This phenomenon generates an alternating current on the surface of the antenna, which flows toward the gap of the antenna. SPPs propagate as electromagnetic waves along the metal–dielectric interface, but their amplitude diminishes exponentially. In metals, this decay is more rapid because of the absorption losses, whereas in the dielectric layer, the SPPs signal attenuates gradually. Consequently, a nonlinear relationship is observed between the antenna's length and its frequency in a plasmonic device, unlike in RF/microwave antennas, where the size is determined solely by frequency.

As the frequency approaches the THz band, the electric field penetrates deeper into the metal owing to the decreased conductivity of conductors. Therefore, the electrical behavior of the metal is characterized by a complex permittivity $\epsilon_c(\omega) = \epsilon'(\omega) + i\epsilon''(\omega)$, which varies with the frequency. The real part $\epsilon'(\omega)$ represents the energy stored in the medium, while the imaginary part $\epsilon''(\omega)$ corresponds to the energy loss within the medium. The loss tangent or dissipation factor δ, defined as ϵ''/ϵ', quantifies the signal loss as it propagates through the medium. At the nanometric scale, there is a distinct relationship between the excitation and charge responses.

Table II reports the real and imaginary parts of ϵ_c for gold at mid-infrared [13]. In this band, gold is preferred because of its convenient complex permittivity as well as for its great chemical stability compared with other noble metals [14].

The complex permittivity is also linked to its conductivity through the relation $\epsilon_c = \epsilon_\infty + (i\sigma/\omega\epsilon_0)$ with ϵ_0 permittivity in vacuum. At mid-infrared frequencies, the complex equation

TABLE II
REAL AND IMAGINARY PARTS OF ELECTRICAL CONDUCTIVITY AT MID-INFRARED RANGE

Conductor type	ϵ'	ϵ''
Gold (Au)	-5605.6	2243.2

TABLE III
REAL AND IMAGINARY PARTS OF COMPLEX PERMITTIVITY AT MID-INFRARED RANGE

Conductor type	σ' (S/m)	σ'' (S/m)
Gold (Au)	0.33728×10^7	-0.84305×10^7

of electrical conductivity of gold is given by the Drude model [13]

$$\sigma = \sigma' + i\sigma'' = \epsilon_0\epsilon''\omega + i\epsilon_0\left(\epsilon' - 1\right)\omega. \tag{2}$$

Table III reports the real and imaginary parts of σ for gold in the mid-IR range. The values in Tables II and III were set in CST Studio Suite to carry out the calculations based on the Drude model.

Interaction with IR waves generates plasmonic modes that influence the size of IR/optical antennas, which depend not only on the geometry but also on the plasmonic effects related to the metal and its environment. Accordingly, the size of a nanoantenna follows a wavelength-scaling rule, where the effective wavelength λ_{eff} governs the size, rather than the actual wavelength, with λ_{eff} smaller than λ. This relationship can be derived from a simple dipole antenna model [15], [16], [17]

$$\lambda_{\text{eff}} = n_1 + n_2\frac{\lambda}{\lambda_p} \tag{3}$$

where λ_{eff} is the effective wavelength scaling for plasmonic antennas, $\lambda_p = (2\pi c/\omega_c)$ is the plasma wavelength of the metal, with c is the speed of light and ω_c is the electron plasma frequency, and n_1 and n_2 are parameters that depend on both the geometry and the dielectric properties of the material. These parameters can be calculated for gold ($\lambda_p = 137$ nm), as follows:

$$n_1 = -R\left(24 + 0.75\frac{\epsilon_\infty}{\epsilon_S}\right) \tag{4}$$

$$n_2 = 0.75\frac{R}{\epsilon_S}\sqrt{\epsilon_\infty + 141.04\epsilon_S} \tag{5}$$

where R represents the radius of a dipole antenna, ϵ_∞ is the high-frequency permittivity, and ϵ_S is the permittivity of the surrounding dielectric environment.

Starting from a desired resonance frequency equal to 5.1 THz, a value of $\lambda_{\text{eff}}/2 = 46.48$ μm for the butterfly nanoantenna length is obtained according to (3). For a length L of 46.48 μm, an optimum width W value of 22.40 μm and an optimum bow angle Θ of 70.79° were obtained using 3-D CST Studio Suite 2023. The optimum geometric parameters of the designed butterfly nanoantenna are presented in Table IV.

Fig. 2 shows the real and imaginary parts of Z_{11} versus frequency in the range 1–7 THz. Three different resonance frequency at 2.1, 3.6, and 5.1 THz are obtained with a -10-dB S_{11} approximately equal to -21, -20, and -18 dB, respectively. An analytical description of the resonances of plasmonic nanoantennas has been well discussed in the literature [18].

The far field at the three resonance frequencies is shown in Fig. 3. The electric field at 2.1 THz is shown in Fig. 4. Table V lists the optimal performance of the butterfly nanoantenna. The values of Z_{11} (Ω), S_{11} (dB), directivity (dBi), and electric field (V/μm) at the resonance frequencies 2.1 THz, 3.6 THz, 5.1 THz, are reported.

TABLE IV
GEOMETRIC PARAMETERS FOR THE BUTTERFLY NANOANTENNA

Length (μm)	Width (μm)	Gap (nm)	Thickness (nm)	Substrate (Silicon + Gold) (nm)
46.48	22.40	20	200	3000 + 50

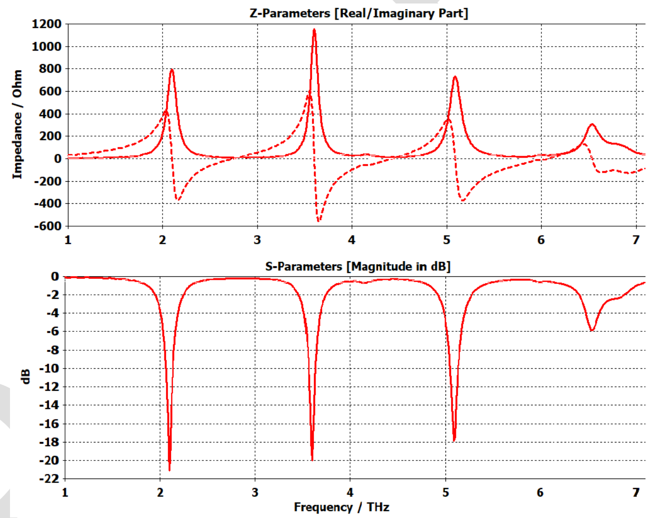

Fig. 2. Z_{11} and S_{11} versus frequency for butterfly nanoantenna.

TABLE V
BUTTERFLY NANOANTENNA PERFORMANCE IN TERMS OF Z_{11}, S_{11}, DIRECTIVITY, AND ELECTRIC FIELD

f_{res} (THz)	Z_{11} (Ω)	S_{11} (dB)	Directivity (dBi)	Electric Field (V/μm)
2.1	774.64	-21.044	5.931	165.092
3.6	1154.43	-20.012	5.699	218.576
5.1	732.27	-17.877	11.04	172.598

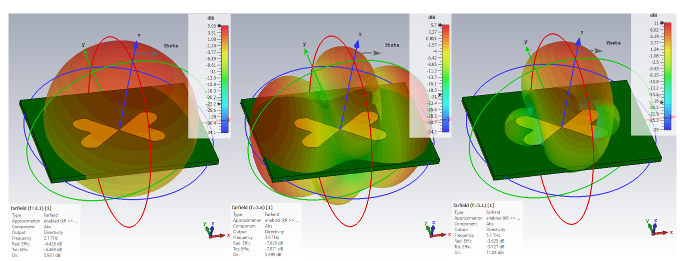
Fig. 3. Far field at 2.1, 3.6, and 5.1 THz for the butterfly nanoantenna.

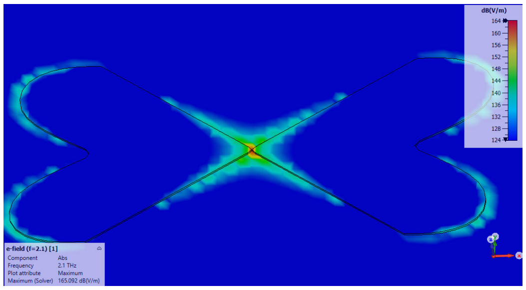

Fig. 4. Electric field for the butterfly nanoantenna at 2.1 THz.

TABLE VI
GAP DISTANCE PARAMETRIC ANALYSIS

Gap (nm)	f_{res} (THz)	Directivity (dBi)	Electric Field (V/m)
20	2.1	5.931	$1.79e\times10^8$
20	3.6	5.699	$2.18e\times10^8$
20	5.1	11.04	$1.72e\times10^8$
40	2.1	6.176	$4.67e\times10^7$
40	3.6	5.723	$4.54e\times10^7$
40	5.1	11.22	$4.48e\times10^7$
80	2.1	6.165	$4.84e\times10^7$
80	3.6	5.673	$4.72e\times10^7$
80	5.1	11.16	$4.66e\times10^7$

TABLE VII
LENGTH L AND WIDTH W PARAMETRIC ANALYSIS

Length (μm)	Width (μm)	f_{res1} (THz)	f_{res2} (THz)	f_{res3} (THz)
36.00	20.00	2.5	4.2	6.1
46.48	22.40	2.1	3.6	5.1
66.00	36.00	1.5	2.6	3.7

A. Parametric Analysis

This section presents a parametric analysis of the nanoantenna design. The results of the gap distance parameter analysis are listed in Table VI. By increasing the value of the gap, an increase in the directivity and a decrease in the electric field at the three frequencies of interest occur. Because the decrease in the electric field is much more significant than the increase in directivity, a value of 20 nm was chosen for the gap based on parametric analysis. Table VII presents the results of the parametric analysis in terms of length and width. Starting from the length value calculated using (2), decreasing the length to a value equal to 36 μm, the resonance frequencies f_{res} of 2.1, 3.6, and 5.1 THz shift to the right, assuming the values 2.5, 4.2, and 6.1 THz, respectively. By increasing the length to a value equal to 66 μm, the resonance frequencies f_{res} of 2.1, 3.6, and 5.1 THz shift to the left, assuming values 1.5, 2.6, and 3.7 THz, respectively.

III. 2 × 2 BUTTERLY NANOANTENNA ARRAY DESIGN AND SIMULATION

Starting from the design of a single butterfly nanoantenna resonating at three desired frequencies (2.1, 3.6, and 5.1 THz), a 2×2 array was designed. Fig. 5 shows the real and imaginary parts of Z_{11} and S_{11}. The resonance frequencies of the array exhibited no shift. Fig. 6 shows the far field at the three resonance frequencies. Table VIII presents the performance of the array in terms of Z_{11}, S_{11}, and the directivity.

TABLE VIII
PERFORMANCE OF THE ARRAY IN TERMS OF Z_{11}, S_{11}, AND DIRECTIVITY

f_{res} (THz)	Z_{11} (Ω)	S_{11} (dB)	Directivity (dBi)
2.1	837.87	-34.4	9.81
3.6	1206.82	-14	12.32
5.1	754.78	-28.5	12.91

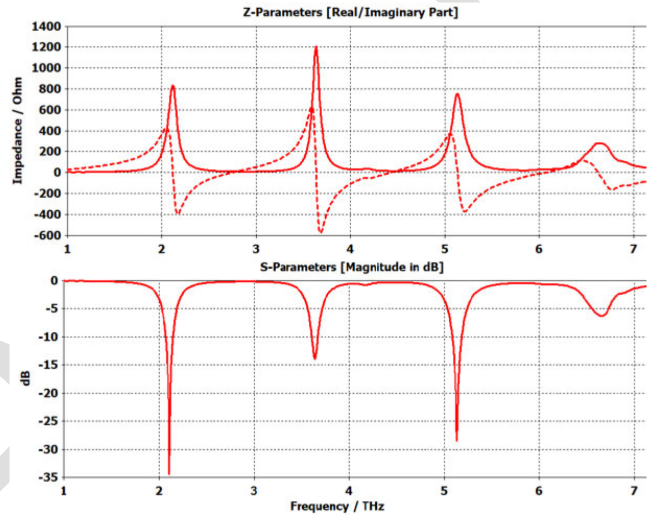

Fig. 5. Z_{11} and S_{11} versus frequency for butterfly nanoantenna array.

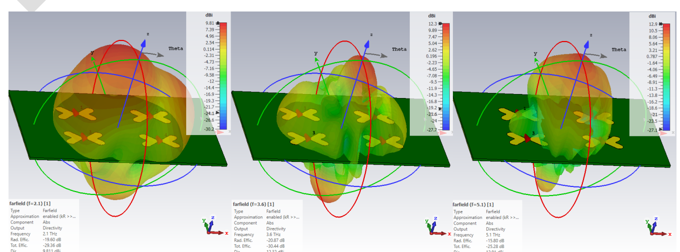

Fig. 6. Butterfly array far-field and directivity.

IV. SHAMROCK ANTENNA DESIGN AND SIMULATION

To obtain a plasmonic nanoantenna-based sensor resonating at all five resonance frequencies reported in Table I, considering that the butterfly nanoantenna had only three resonance frequencies, 2.1, 3.6, and 5.1 THz, a modified structure for the butterfly nanoantenna was studied to resonate at 1.9 and 3.3 THz, respectively.

Fig. 7 shows the CST schematic model of the novel modified butterfly geometry called the shamrock nanoantenna. It presents three equal arms with length $L/2$, width W, flare angle Θ, and gap G.

Table IX lists all geometric parameters for the shamrock nanoantenna with the same substrate as the butterfly nanoantenna.

Fig. 8 shows the real and imaginary parts of Z_{11} versus frequency in the range of 1–7 THz. Two different resonance

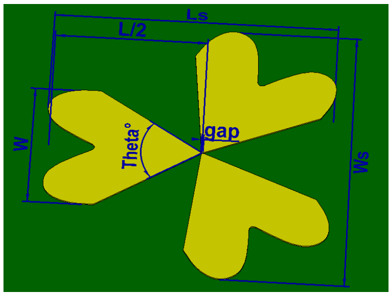

Fig. 7. CST schematic model of the novel proposed shamrock nanoantenna.

TABLE IX
GEOMETRIC PARAMETERS FOR THE SHAMROCK NANOANTENNA

L/2 (μm)	W (μm)	Ls (μm)	Ws (μm)	gap (nm)
23.2	22.4	43	48.8	20

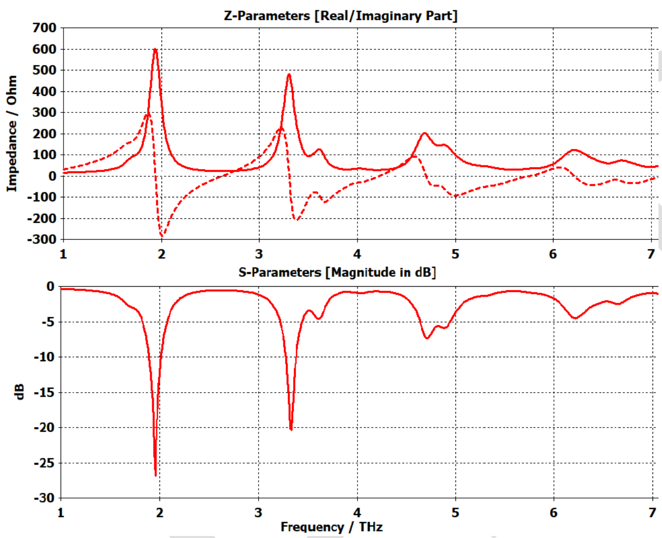

Fig. 8. Z_{11} and S_{11} versus frequency for the shamrock nanoantenna.

TABLE X
PERFORMANCE OF THE SINGLE SHAMROCK NANOANTENNA IN TERMS OF Z_{11}, S_{11}, DIRECTIVITY, AND ELECTRIC FIELD

f_{res} (THz)	Z_{11} (Ω)	S_{11} (dB)	Directivity (dBi)	Electric Field (V/μm)
1.9	595.60	-26.81	5.667	163.021
3.3	469.57	-20.36	6.514	206.524

frequencies at 1.9 and 3.3 THz with a −10-dB S_{11} equal to approximately −26.81 and −20.36 dB, respectively, occur.

The far field at the two resonance frequencies is shown in Fig. 9. Fig. 10 shows the electric field at 1.9 THz. The performance of the shamrock nanoantenna is listed in Table X.

V. 2 × 2 SHAMROCK ANTENNA ARRAY DESIGN AND SIMULATION

Beginning with the design of a single shamrock nanoantenna, a 2 × 2 array was designed, as shown in Fig. 11.

Fig. 12 shows the real and imaginary parts of Z_{11} and S_{11}. Fig. 13 shows the far field at the two frequencies, and the performance of the array is presented in Table XI.

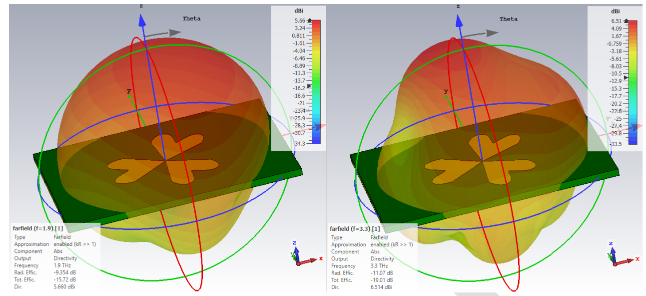

Fig. 9. Far field at 1.9 and 3.3 THz for the shamrock nanoantenna.

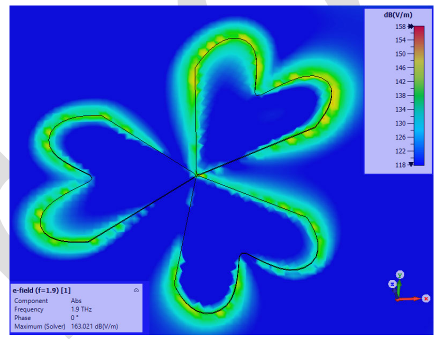

Fig. 10. Electric field for the shamrock nanoantenna.

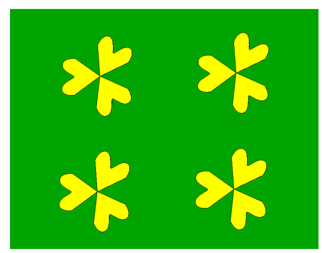

Fig. 11. 2 × 2 shamrock array design.

TABLE XI
PERFORMANCE OF THE SHAMROCK ARRAY IN TERMS OF Z_{11}, S_{11}, AND DIRECTIVITY

f_{res} (THz)	Z_{11} (Ω)	S_{11} (dB)	Directivity (dBi)
1.9	730.77	-13.91	6.768
3.3	637.11	-18.36	7.208

VI. COMPARISON BETWEEN BUTTERFLY AND SHAMROCK NANOANTENNAS AND CLASSIC BOWTIE NANOANTENNAS

Fig. 14 shows a classic bowtie with a gap 20 nm and dimensions equal to those of a previously designed butterfly. In Fig. 15, the real and imaginary parts of Z_{11} and S_{11} versus the frequency over the 1–7-THz range for the classic bowtie nanoantenna are shown. Three resonance frequencies were obtained; however, only the second and third resonance frequencies corresponded to those listed in Table I. It was not possible to obtain the first resonance frequency corresponding to 1.9 or 2.1 THz. By varying the geometric dimensions of the bowtie nanoantenna according to the parametric analysis reported in Section II, all three frequencies shifted to the right

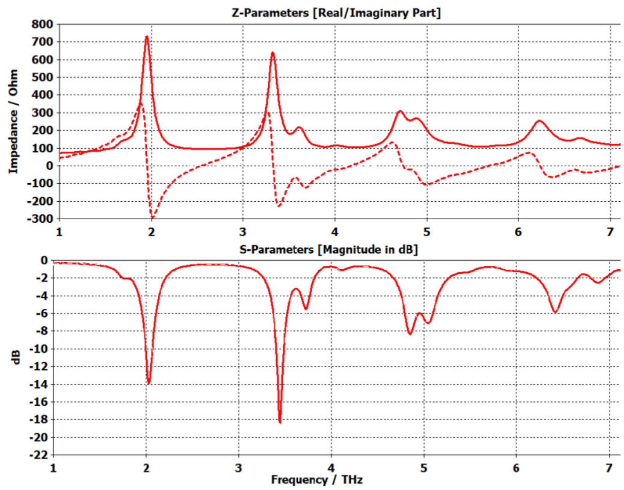

Fig. 12. Z_{11} and S_{11} versus frequency for the shamrock nanoantenna array.

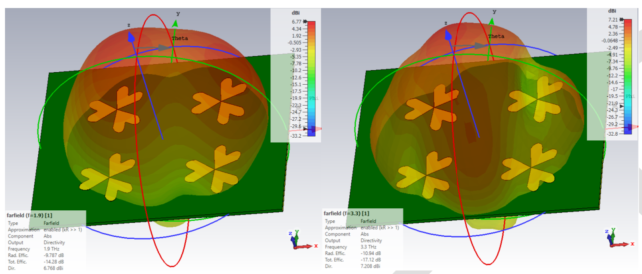

Fig. 13. Far field at 1.9 and 3.3 THz for the shamrock array.

TABLE XII
BOWTIE NANOANTENNA PERFORMANCE IN TERMS OF Z_{11}, S_{11}, DIRECTIVITY, AND ELECTRIC FIELD

f_{res} (THz)	Z_{11} (Ω)	S_{11} (dB)	Directivity (dBi)	Electric Field (V/µm)
2	613	-12.38	5.750	166.39
3.6	902	-25.48	4.144	169.96
5.1	690	-14.73	8.357	169.09

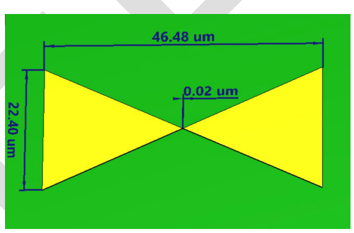

Fig. 14. CST schematic model of a bowtie nanoantenna.

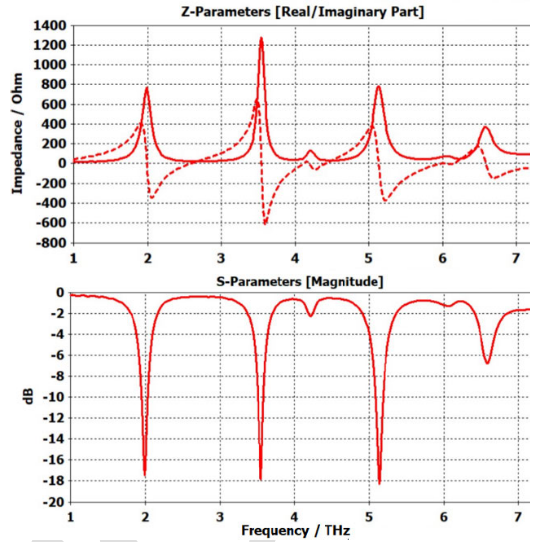

Fig. 15. Z_{11} and S_{11} for the bowtie nanoantenna.

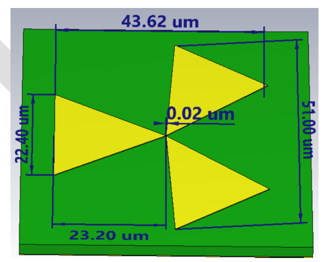

Fig. 16. CST schematic model of the bowtie nanoantenna with three arms.

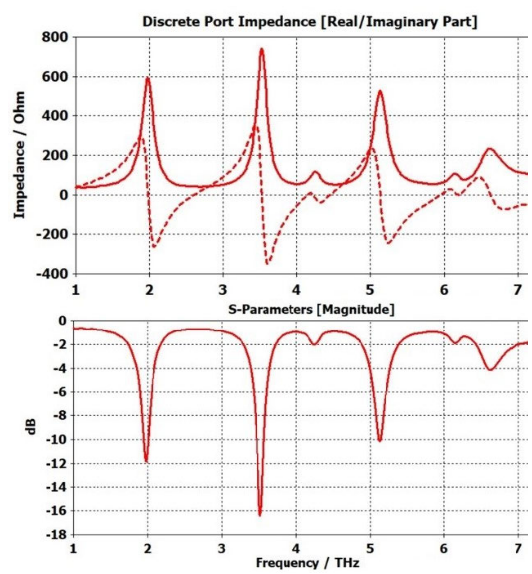

Fig. 17. Z_{11} and S_{11} for three-arm bowtie nanoantenna.

or left. Table XII lists Z_{11}, S_{11}, directivity, and electric field for the three resonance frequencies.

The CST schematic model of the simulated bowtie nanoantenna with three arms is shown in Fig. 16.

The graphs of Z_{11} and S_{11}, in Fig. 17, show the same resonance frequencies as the single classic bowtie, unlike the shamrock nanoantenna, which has two different resonance frequencies compared with the butterfly nanoantenna. Furthermore, the three-arm bowtie shows a worsening of the S_{11} values.

Table XIII presents the characteristics of the three-arm classic bowtie nanoantenna in terms of Z_{11}, S_{11}, directivity, and the electric field.

The Q factors for butterfly, shamrock, and bowtie nanoantennas are calculated by considering a series RLC equivalent circuit model, where L, C, and R, represent the kinetic

TABLE XIII
PERFORMANCE SINGLE THREE-ARM BOWTIE IN TERMS OF Z_{11}, S_{11}, DIRECTIVITY, AND ELECTRIC FIELD

f_{res} (THz)	Z_{11} (Ω)	S_{11} (dB)	Directivity (dBi)	Electric Field (V/μm)
2	597.48	-11.91	5.942	157.833
3.6	736.24	-16.38	4.651	158.398
5.1	524.32	-10.12	8.626	158.291

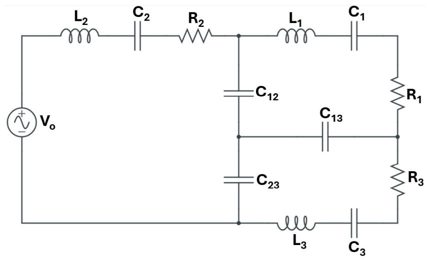

Fig. 18. *RLC* equivalent circuit model for a butterfly nanoantenna.

TABLE XIV
Q-FACTOR VALUE FOR BUTTERFLY, SHAMROCK, AND BOWTIE NANOANTENNAS

Nanoantenna	$Q_{(1.9)}$	$Q_{(2.1)}$	$Q_{(3.3)}$	$Q_{(3.6)}$	$Q_{(5.1)}$
Butterfly		17.94		36.36	32.39
Shamrock	10.61		18.75		
Bowtie				18.68	21.37

inductance due to the inertia of the oscillating electrons, the capacitive coupling between different parts of the nanoantenna or between the nanoantenna and the surrounding medium, and the losses due to radiative and nonradiative damping, respectively, and depend on the geometry of the nanoantenna and the material properties of the metal and the surrounding dielectric.

Fig. 18 shows the *RLC* equivalent circuit for the butterfly nanoantenna. The circuit consists of three loops of resistive, inductive, and capacitive elements coupled with capacitive elements [20]. Each loop corresponded to a single plasmonic resonance. The combination of inductive and capacitive elements in each loop generates a resonance, whereas the resistive element accounts for energy dissipation (due to radiation and ohmic loss). The model for the *RLC* circuit is based on the resonance frequency formula for a series *RLC* circuit, which is given by

$$f_{\text{res}} = \frac{1}{2\pi\sqrt{\text{LC}}}. \quad (6)$$

The Q factor of the *RLC* circuit can be calculated using the following equation:

$$Q = \frac{f_{\text{res}}}{\Delta f}. \quad (7)$$

The Q-factor values for the butterfly, shamrock, and bowtie nanoantennas are listed in Table XIV, which shows that the butterfly and shamrock nanoantennas present a higher Q factor than the classic bowtie nanoantennas.

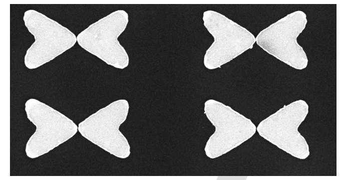

Fig. 19. Fabricated 2 × 2 butterfly nanoantennas array.

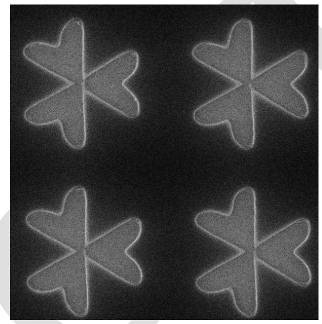

Fig. 20. Fabricated 2 × 2 shamrock nanoantennas array.

VII. SENSING AND DETECTION OF VARIOUS MOLECULES

Regarding the sensing task, the nanoantenna-based sensor can detect several molecules that have resonance peaks associated with the same molecules as the nanoantennas.

Figs. 19 and 20 show the images of the fabricated 2 × 2 array of the proposed nanoantennas (butterfly and shamrock) under a scanning electron microscope. The combination of the two proposed antennas allows us to address the spectrum of interest and can recognize various material crimes and narcotic substances of various types. The resonance frequencies of illegal materials with the corresponding proposed nanoantennas are listed in Table XV [3].

Fig. 21 shows a generic correspondence between the results of the numerical simulation and the generic experimental simulation using MDMA, also called "Ecstasy." MDMA is a psychoactive substance belonging to the phenethylamine class and is known for its entactogenic effects, although it is not strictly psychedelic. It is a semisynthetic compound commonly derived from safrole [21]. It is one of the most widespread narcotics and is typically consumed in the form of tablets or crystals, dissolved in liquids, or less commonly smoked. MDMA abuse can pose health risks both physically and mentally, with experimental evidence indicating neurotoxicity [22]. Detection with plasmonic nanoantenna-based sensors is a completely nondestructive method, because it is sufficient to place a few drops on the device to analyze the sample via Fourier transform infrared spectroscopy, a technique used to obtain the infrared absorption or emission spectrum of a solid, liquid, or gas [23], [25]. To achieve this, the material must be dissolved in a neutral solution to avoid altering the pH. A few drops must be applied to a plasmonic sensor.

The sensitivity of the proposed nanoantennas, calculated as the shift in the resonance frequency per refractive index unit (RIU) of the target material, was evaluated using the finite-element method (FEM) implemented in ANSYS HFSS

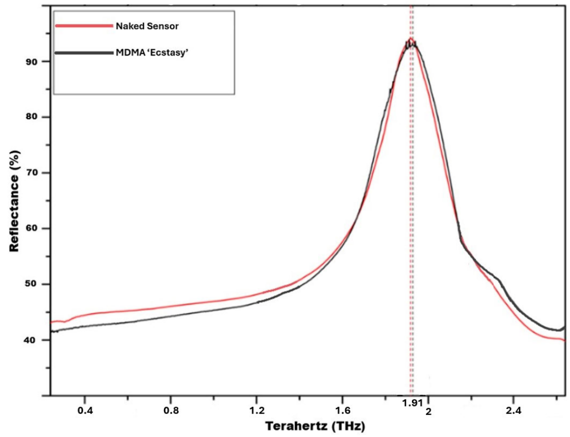

Fig. 21. Numerical and experimental data for MDMA (Ecstasy) [4].

TABLE XV
MATCHING BETWEEN NANOANTENNAS AND ILLICIT MATERIALS AND DRUGS

f_{res}	Material	Matched Nanoantenna
1.9	PE4,HMX,TNT,MDMA	Shamrock
2.1	SEMTEX-H	Butterfly
3.3	Lactose a-monohydrate,Terfenadine	Shamrock
3.6	Co-Codamol	Butterfly
5.1	Naproxen sodium,Caffeine	Butterfly

TABLE XVI
PERFORMANCE OF BUTTERFLY AND SHAMROCK NANOANTENNAS IN SENSITIVITY GHz/RIU WITH 1 μM OF ANALYTE

f_{res} (THz)	$\Delta n = 0.01$ RIU (THz)	Δf (GHz)	Sensitivity (GHz/ RIU)	Analyte Thickness (µm)
1.9	1.91	10	1000	1
2.1	2.12	20	2000	1
3.3	3.35	50	5000	1
3.6	3.69	90	9000	1
5.1	5.20	100	10000	1

software. The shift in resonance frequency owing to the presence of the target material indicates the antenna's ability to detect the material. The sensitivity values for the resonance frequencies 1.9, 2.1, 3.3, 3.6, and 5.1 THz, for both drugs and explosives, and with an analyte thickness value equal to 1 μm, are listed in Table XVI. The calculated values show a great ability of butterfly and shamrock nanoantennas to distinguish between the presence and the absence of target materials at the given frequencies. In Table XVII, the sensitivity values for the resonance frequencies 1.9, 2.1, 3.3, 3.6, and 5.1, with an analyte thickness value equal to 5 μm, are listed. The sensitivity of the antennas shows significant variations in resonance frequencies for a given change in the refractive index.

In Table XVIII, a comparison of our work with state-of-the-art similar works in terms of sensitivity is reported. The average sensitivity is calculated using the following formula:

$$\text{Average sensitivity} = \frac{\sum_{i=1}^{N} S_i}{N}$$

where S_i represents the sensitivity at each specific resonance frequency and N is the total number of frequencies.

TABLE XVII
PERFORMANCE OF BUTTERFLY AND SHAMROCK NANOANTENNAS IN SENSITIVITY GHz/RIU WITH 5 μM OF ANALYTE

f_{res} (THz)	$\Delta n = 0.01$ RIU (THz)	Δf (GHz)	Sensitivity (GHz/ RIU)	Analyte Thickness (µm)
1.9	1.915	15	1500	5
2.1	2.125	25	2500	5
3.3	3.36	60	6000	5
3.6	3.70	100	10000	5
5.1	5.215	115	11500	5

TABLE XVIII
PERFORMANCE COMPARISON OF OUR WORK WITH OTHER SIMILAR THz SENSORS

Ref.	Size (μm$\times\mu$m)	f_{res} (THz)	Sens. (GHz/ RIU)	Avg. Sens. (GHz/ RIU)	Analyte Thickness (µm)
[26]	36 x 36	2.2	300	296	1
[27]	15 x 15	4.8	2020	1936	1
Shamrock	46 x 22	3.3	5000	3375	1
[28]	36 x 36	5.9	2000	1800	5
[27]	15 x 15	4.8	3800	1936	5
Butterfly	46 x 22	5.1	11500	7500	5

The shamrock and butterfly nanoantennas exhibit the highest values of average sensitivity 3375 (GHz/RIU) and 7500 (GHz/RIU), for two different analyte thickness values, 1 and 5 μm, respectively, when compared with state-of-the-art similar works.

The measurement setup was composed of a Perkin-Elmer spectrum one Fourier-transform infrared (FTIR) spectrometer, which allows for 10× optical and 15× IR magnifications for the detection of the molecules. All the spectra obtained during the experiments were automatically normalized against a background spectrum from a flat, unpatterned gold layer of identical thickness to the nanostructures deposited on the same substrate. In general, more than 100 scans were conducted with an acquisition time of 5 s each.

Figs. 22 and 23 show the absorbance and reflectance characteristics of butterfly and shamrock nanoantennas, respectively. The points of interest are the three resonance frequencies, which show that there is a large peak in the sensitivity. This is why the nanoantenna can detect molecules in very small quantities as long as they are in the same resonance range. The sensor can be seamlessly integrated with micrometer scale channels, making it suitable for the high-sensitivity and real-time analysis of IR-emitting samples. This is particularly valuable in contexts in which IR spectroscopy is significantly hindered by the absorption bands of liquid water. Such applications are crucial in fields, such as environmental monitoring, biomedical diagnostics, and chemical processing, where the accurate detection and analysis of trace elements or contaminants are required. The development of a new plasmonic sensing method is proposed for use as a window in FTIR spectrometry, along with an innovative accessory that can operate in either the reflection or transmission mode. This approach offers a method for identifying the presence of at least one contaminant in a physical sample by using a spectrometer. The proposed plasmonic platform enhances

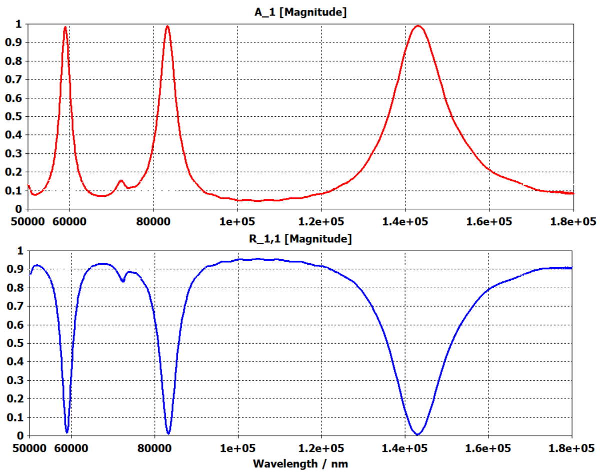

Fig. 22. Absorbance and reflectance versus wavelength for the butterfly nanoantenna.

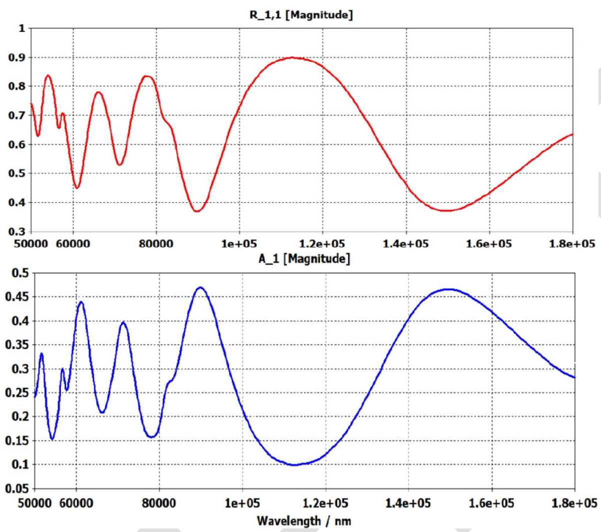

Fig. 23. Absorbance and reflectance versus wavelength for the shamrock nanoantenna.

infrared sensing capabilities by utilizing FTIR spectroscopy to provide precise and reliable detection and analysis of various substances [29].

The plasmonic sensor works by exploiting surface plasmon resonance (SPR), which amplifies the interaction between IR light and the sample, thereby increasing the sensitivity and specificity of spectrometric measurements. This method is particularly useful for detecting low-concentration analytes that are, otherwise, difficult to identify using conventional IR spectroscopy [30].

In practical applications, the integration of this plasmonic platform with microfluidic channels allows for the continuous flow of samples, thereby facilitating real-time monitoring and analysis. Moreover, the ability of the accessory to function in both reflection and transmission modes provides versatility in sample analysis. Thus, the reflection mode is advantageous when dealing with opaque samples or when the surface characteristics are of interest, whereas the transmission mode is useful for transparent or thin samples and offers more comprehensive data collection. Overall, the introduction of this plasmonic platform and its accessory into FTIR spectrometry represents a significant advancement, promising enhanced analytical performance and broader application potential across various scientific and industrial domains.

To quantify the surface-enhanced infrared absorption (SEIRA) sensitivity, the enhancement factor (EF), which compares the enhanced signal strengths to standard IR techniques, is considered

$$\mathrm{EF} = \frac{\Delta R}{\Delta R_0} \cdot \frac{A_0}{A_{\mathrm{SEIRA}}} \tag{8}$$

where ΔR is the difference in the reflectance values with and without the molecules, ΔR_0 is the reflectance difference with a flat gold layer of the same thickness as the nanoantennas acquired under the same conditions, A_{SEIRA} is the area with molecules in SEIRA measurements, and A_0 is the area in reference measurements. The active area A_{SEIRA} mainly originates from molecules in the antenna hotspots. An approximation of the active area is the surface of the gap, although this is approximate if the nanoantennas with the substrate are uniformly covered with analytes [31]. By analyzing an area A_0 of 200×200 μm^2, corresponding to a 2×2 nanoarray, with an A_{SEIRA} of 2×10^8 nm^2, ΔR_0 is 4.93×10^{-9} calculated on a 200×200 μm^2 gold sample of the exact same thickness as the nanoantennas, and ΔR which is 15% of the variation between the measurement with and without the molecule, an EF of approximately 6.09×10^5 is obtained.

VIII. Conclusion

In this study, a novel plasmonic sensing method utilizing two distinct nanoantennas, namely, the butterfly-shaped and shamrock-shaped nanoantennas, has been proposed. These nanoantennas, when used jointly as standalone sensors, demonstrate remarkable capabilities for detecting illicit substances within the near-infrared spectrum. Their adaptability and efficacy extend into the challenging THz frequency range, positioning them as promising candidates for future nondestructive sensing technologies.

Moreover, the integration of multiband THz capabilities enhances their utility in various applications, including the detection of chemotherapeutic drugs in cancer treatment [32] and cancer DNA [33]. This advancement underscores the potential of plasmonic nanoantenna-based sensors to revolutionize advanced sensing methodologies by offering enhanced sensitivity and specificity.

Recent advancements have highlighted the efficacy of multiband THz sensors in biomedical applications. These sensors offer precise and reliable detection outcomes across various fields, showing their potential impact on scientific research and practical applications [34]. The integration of novel nanoantenna designs, coupled with multiband THz sensing capabilities, represents a significant leap forward in sensor technology. Such innovations have profound impacts on advanced sensing methodologies, paving the way for enhanced sensitivity and specificity for various sensing applications.

In conclusion, the development of multiband THz sensors marks a critical advancement in sensor technology, poised to revolutionize detection capabilities and expand the horizons of sensing technologies in the future.

References

[1] M. O. AlNabooda, R. M. Shubair, N. R. Rishani, and G. Aldabbagh, "Terahertz spectroscopy and imaging for the detection and identification of illicit drugs," in *Proc. Sensors Netw. Smart Emerg. Technol. (SENSET)*, Beirut, Lebanon, Sep. 2017, pp. 1–4, doi: 10.1109/SENSET.2017.8125065.

[2] J. F. Federici et al., "THz imaging and sensing for security applications—Explosives, weapons and drugs," *Semiconductor Sci. Technol.*, vol. 20, no. 7, pp. S266–S280, Jul. 2005, doi: 10.1088/0268-1242/20/7/018.

[3] K. S. Kalasinsky, "Terahertz frequency spectroscopy and its potential for security applications," in *Infrared and Raman Spectroscopy in Forensic Science*, A. D. Burnett, J. E. Cunningham, A. G. Davies, P. Dean, and E. H. Linfield, Eds., Hoboken, NJ, USA: Wiley, 2012, pp. 295–314.

[4] D. G. Allis, P. M. Hakey, and T. M. Korter, "The solid-state terahertz spectrum of MDMA (Ecstasy)—A unique test for molecular modeling assignments," *Chem. Phys. Lett.*, vol. 463, nos. 4–6, pp. 353–356, Oct. 2008.

[5] A. Kasal, M. Budesinsky, and W. J. Griffiths, "Spectroscopic methods of steroid analysis," in *Steroid Analysis*, H. L. J. Makin, D. B.Gower, and D. N. Kirk, Eds., Dordrecht, The Netherland: Springer, 2010, pp. 25–113.

[6] M. O. A. Malik, X. Ren, C.-M. Hsieh, Y. Zhang, and Q. Liu, "Investigation of equivalence between non-resonant Raman excitation spectroscopy and conventional Raman spectroscopy," *IEEE J. Sel. Topics Quantum Electron.*, vol. 29, no. 4, pp. 1–9, Jul. 2023, doi: 10.1109/JSTQE.2022.3185735.

[7] J. A. Schuller, E. S. Barnard, W. Cai, Y. C. Jun, J. S. White, and M. L. Brongersma, "Plasmonics for extreme light concentration and manipulation," *Nature Mater.*, vol. 9, no. 3, pp. 193–204, Mar. 2010.

[8] D. K. Gramotnev and S. I. Bozhevolnyi, "Plasmonics beyond the diffraction limit," *Nature Photon.*, vol. 4, no. 2, pp. 83–91, 2010.

[9] V. Aglieri et al., "Improving nanoscale terahertz field localization by means of sharply tapered resonant nanoantennas," *Nanophotonics*, vol. 9, no. 3, pp. 683–690, Feb. 2020, doi: 10.1515/nanoph-2019-0459.

[10] V. Di Meo et al., "Probing denaturation of protein a via surface-enhanced infrared absorption spectroscopy," *Biosensors*, vol. 12, no. 7, p. 530, Jul. 2022, doi: 10.3390/bios12070530.

[11] M. K. Anam and S. Choi, "Bowtie nanoantenna array integrated with artificial impedance surfaces for realizing high field enhancement and perfect absorption simultaneously," *IEEE Access*, vol. 8, pp. 99858–99869, 2020, doi: 10.1109/ACCESS.2020.2997680.

[12] M. J. Dodd and A. Z. Elsherbeni, "Bowtie antenna with integrated matching network for wideband and circular polarization," in *Proc. IEEE Int. Symp. Antennas Propag. USNC-URSI Radio Sci. Meeting (USNC-URSI)*, Portland, OR, USA, Jul. 2023, pp. 1531–1532, doi: 10.1109/usnc-ursi52151.2023.10238178.

[13] W. Amara et al., "Analysis of infrared nano-antennas material properties for solar energy collection," *Appl. Comput. Electromagn. Soc. J.*, vol. 35, pp. 258–266, Mar. 2020.

[14] A. Chekini, S. Sheikhaei, and M. Neshat, "Nanoantenna arrays as diode-less rectifiers for energy harvesting in mid-infrared band," *Microw. Opt. Technol. Lett.*, vol. 61, no. 2, pp. 412–416, Feb. 2019, doi: 10.1002/mop.31562.

[15] P. Biagioni, J. Huang, and B. Hecht, "Nanoantennas for visible andinfrared radiation," *Rep. Prog. Phys.*, vol. 75, no. 2, 2012, Art. no. 024402.

[16] I. S. Maksymov, I. Staude, A. E. Miroshnichenko, and Y. S. Kivshar, "Optical Yagi–Uda nanoantennas," *Nanophotonics*, vol. 1, no. 1, pp. 65–81, Jul. 2012.

[17] L. Mescia and A. Massaro, "New trends in energy harvesting from Earth long-wave infrared emission," *Adv. Mater. Sci. Eng.*, vol. 2014, pp. 1–10, Jan. 2014.

[18] A. Locatelli, "Peculiar properties of loop nanoantennas," *IEEE Photon. J.*, vol. 3, no. 5, pp. 845–853, Oct. 2011.

[19] S. Rakheja, P. Sengupta, and S. M. Shakiah, "Design and circuit modeling of graphene plasmonic nanoantennas," *IEEE Access*, vol. 8, pp. 129562–129575, 2020, doi: 10.1109/ACCESS.2020.3009206.

[20] M. Amin and H. Bağci, "Investigation of Fano resonances induced by higher order plasmon modes on a circular nano-disk with an elongated cavity," *Prog. Electromagn. Res.*, vol. 130, pp. 187–206, 2012, doi: 10.2528/pier12040507.

[21] B. H. Morimoto, S. Lovell, and B. Kahr, "Ecstasy: 3,4-methylenedioxymethamphetamine (MDMA)," *Acta Crystallographica Sect. C, Cryst. Struct. Commun.*, vol. 54, no. 2, pp. 229–231, 1998.

[22] H. Kim, K. W. Kim, J. Park, J. K. Han, and J. Son, "Terahertz tomographic imaging of topical drugs," in *Conf. Lasers Electro-Opt., OSA Tech. Dig.* Optica Publishing Group, 2012, Paper JW2A.48.

[23] Q. Pei, X. Zheng, J. Tan, Y. Luo, and S. Ye, "Probing the local near-field intensity of plasmonic nanoparticles in the mid-infrared spectral region," *J. Phys. Chem. Lett.*, vol. 15, no. 20, pp. 5390–5396, May 2024, doi: 10.1021/acs.jpclett.4c00964.

[24] F. Neubrech, C. Huck, K. Weber, A. Pucci, and H. Giessen, "Surface-enhanced infrared spectroscopy using resonant nanoantennas," *Chem. Rev.*, vol. 117, no. 7, pp. 5110–5145, Apr. 2017, doi: 10.1021/acs.chemrev.6b00743.

[25] C. D'Andrea et al., "Optical nanoantennas for multiband surface-enhanced infrared and Raman spectroscopy," *ACS Nano*, vol. 7, no. 4, pp. 3522–3531, Apr. 2013.

[26] A. S. Saadeldin, M. F. O. Hameed, E. M. A. Elkaramany, and S. S. A. Obayya, "Highly sensitive terahertz metamaterial sensor," *IEEE Sensors J.*, vol. 19, no. 18, pp. 7993–7999, Sep. 2019.

[27] A. Veeraselvam, G. N. A. Mohammed, and K. Savarimuthu, "A novel ultra-miniaturized highly sensitive refractive index-based terahertz biosensor," *J. Lightw. Technol.*, vol. 39, no. 22, pp. 7281–7287, Nov. 2021, doi: 10.1109/JLT.2021.3112529.

[28] A. Ma et al., "Ultrasensitive THz sensor based on centrosymmetric F-shaped metamaterial resonators," *Frontiers Phys.*, vol. 8, p. 441, Oct. 2020.

[29] M. Janneh, "(INVITED)Surface enhanced infrared absorption spectroscopy using plasmonic nanostructures: Alternative ultrasensitive on-chip biosensor technique," *Results Opt.*, vol. 6, Jan. 2022, Art. no. 100201, doi: 10.1016/j.rio.2021.100201.

[30] B. T. Cunningham, "Photonic crystal surfaces as a general purpose platform for label-free and fluorescent assays," *JALA: J. Assoc. Lab. Autom.*, vol. 15, no. 2, pp. 120–135, Apr. 2010, doi: 10.1016/j.jala.2009.10.009.

[31] E. K. Herkert, D. R. B. Alvaro, M. Recchia, W. Langbein, P. Borri, and M. F. Garcia-Parajo, "Hybrid plasmonic nanostructures for enhanced single-molecule detection sensitivity," *ACS Nano*, vol. 17, no. 9, pp. 8453–8464, May 2023, doi: 10.1021/acsnano.3c00576.

[32] F. Rodino, M. Bartoli, and S. Carrara, "Simultaneous and selective detection of etoposide and methotrexate with single electrochemical sensors for therapeutic drug monitoring," *IEEE Sensors Lett.*, vol. 7, no. 8, pp. 1–4, Aug. 2023, doi: 10.1109/lsens.2023.3300817.

[33] H. Cheon, H.-J. Yang, S.-H. Lee, Y. A. Kim, and J.-H. Son, "Terahertz molecular resonant of cancer DNA," *Sci. Rep.*, vol. 6, no. 1, 2016, Art. no. 37103.

[34] A. Veeraselvam, G. N. A. Mohammed, K. Savarimuthu, and P. D. Vijayaraman, "An ultra-thin multiband refractive index-based carcinoma sensor using THz radiation," *IEEE Sensors J.*, vol. 22, no. 3, pp. 2045–2052, Feb. 2022, doi: 10.1109/JSEN.2021.3134663.

Marco Scalici received the bachelor's and master's degrees in electronic engineering (modern electronics) from the University of Palermo (UNIPA), Palermo, Italy, in 2020 and 2023, respectively, where he is pursuing the Ph.D. degree in ICT.

He has authored or co-authored the scientific articles about microwave biosensors.

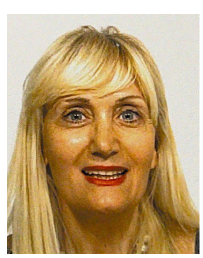

Patrizia Livreri (Senior Member, IEEE) received the Laurea (Hons.) degree in electronics engineering and the Ph.D. degree in electronics and communications engineering from the University of Palermo, Palermo, Italy, in 1986 and 1992, respectively.

She is a Professor at the Department of Engineering, University of Palermo, and a Visiting Professor at San Diego State University, San Diego, CA, USA. From 1993 to 1994, she was a Researcher with CNR, Palermo. She serves as the Scientific Director for the Microwave Instruments and Measurements Laboratory, Department of Engineering, Palermo. She has authored or co-authored the scientific books and more than 250 scientific publications. Her current research interests include microwave power amplifiers, antennas from microwave to terahertz, and microwave quantum radar.